AGU ADVANCING EARTH AND SPACE SCIENCES

Geophysical Research Letters®

RESEARCH LETTER
10.1029/2023GL103435

The Onset of Recrystallization in Polar Firn

Ayobami Ogunmolasuyi[1], Andrii Murdza[1], and Ian Baker[1]

[1]Thayer School of Engineering, Dartmouth College, Hanover, NH, USA

Abstract Constraining the onset of dynamic recrystallization (DRX) and its effects on the mechanical properties of firn is crucial for firn densification modeling. To that end, samples from a depth of 13 m in a Summit, Greenland (72°35′N, 38°25′W) firn core were subjected to creep tests at −14°C and 0.21 MPa compressive stress to strains of 7%, 12%, 18%, and 29%. Microstructural analyses using thin-section imaging and microcomputed x-ray tomography (micro-CT) revealed smaller grain sizes, reduced specific surface area and connectivity, and increased density in relation to reduced porosity as the strain increases. These results show that DRX occurs in firn under creep, with strain-induced boundary migration (SIBM) and nucleation and growth starting at ∼7%. DRX leads to elongated grains, reduced grain size, and the development of a preferred crystallographic orientation, indicating that DRX occurs by both SIBM and nucleation and growth.

Plain Language Summary Firn is multi-year snow that undergoes densification due to the load from the snow overburden and from sintering. Understanding firn densification is important for interpreting ice core records, predicting ice sheet mass balance and elevation changes, and studying climate change effects. Previous densification models focused on accumulation rate and temperature, overlooking the role of recrystallization. To address this gap, compression tests were performed on Greenland firn samples from a depth of 13 m. The deformation resulted in reduced median grain size, preferred crystallographic orientation, and increased density. Our findings indicate that dynamic recrystallization starts when the firn is subjected to a strain of about 7% through boundary migration of old grains, around which new stress-free grains also start to form.

Key Points:

- Dynamic Recrystallization occurs in firn through strain-induced boundary migration, and nucleation and growth
- Average grain size in firn decreases under constant temperature and compressive stress in firn

Supporting Information:

Supporting Information may be found in the online version of this article.

Correspondence to:

I. Baker,
ian.baker@dartmouth.edu

Citation:

Ogunmolasuyi, A., Murdza, A., & Baker, I. (2023). The onset of recrystallization in polar firn. *Geophysical Research Letters*, *50*, e2023GL103435. https://doi.org/10.1029/2023GL103435

Received 27 FEB 2023
Accepted 18 NOV 2023

1. Introduction

Firn is defined as snow that has undergone partial compaction with a density that ranges between that of snow and ice. Firn densification refers to the transformation of snow into glacial ice. A comprehensive understanding of the firn densification process is critical to understanding various processes on glaciers and ice sheets. Ice cores, for instance, contain bubbles that capture the atmospheric composition at the time of bubble formation that can be used to reconstruct past climates (Alley, 2000; Raynaud et al., 1993; Sowers & Bender, 1995), with firn densification controlling the bubble formation process. Moreover, surface meltwater can percolate into the pore spaces in firn, forming firn aquifers which essentially slow or prevent runoff (Forster et al., 2013; Harper et al., 2012). Thus, understanding firn aquifer development will improve estimates of how much surface meltwater will eventually flow into the sea, leading to sea level rise. Additionally, variations in the firn densification rate pose a significant uncertainty in satellite estimates of ice sheet elevation and mass balance changes (Helsen et al., 2008), and information about the firn air content is essential for deriving the mass balance of an ice sheet (Horlings et al., 2021; Oraschewski & Grinsted, 2022).

Firn densification occurs in three stages characterized by the dominant densification mechanism. The first stage is dominated by grain boundary sliding, vapor transport, and surface diffusion until a density of 550 kgm^{-3} (Alley, 1987; Gow, 1975; Maeno & Ebinuma, 1983). In the second stage, pore spaces shrink, limiting vapor diffusion, and leading to sintering processes and recrystallization as the main mechanisms until a density of 830 kgm^{-3} is achieved (Gow, 1975; Maeno & Ebinuma, 1983). The third stage, starting at the firn-ice transition, is dominated by bubble shrinkage and compression until the density of ice is reached (917 kgm^{-3}).

A comprehensive understanding of large-scale implications of firn densification processes requires models to include coupling to the physics, which can be informed by experimental studies. In addition to predicting density, these models help researchers understand how temperature and precipitation changes affect the densification rate of ice. Numerous empirical firn models have been developed and most of them (Barnola et al., 1991; Herron & Langway, 1980) predict density evolution using only accumulation rate and temperature, and assume steady-state processes. However, firn densification is governed by microstructural evolution (Arnaud et al., 2000)

and some models have been developed with microstructural considerations that is, grain-scale physical processes (Alley, 1987; Arnaud et al., 2000), while a third set of models describing firn densification using experimental analysis of rheology have also been developed (Meyer et al., 2020). These models disagree in space and time, and thorough investigations into the microstructural evolution of firn are necessary to improve them (Stevens et al., 2020). Consequently, ongoing efforts aim to develop a physics-based model for firn compaction under various conditions. Microstructural evolution directly affects the mechanical properties and rheology of ice with several mechanisms being involved in the microstructural evolution of ice sheets. Normal grain growth (NGG) increases grain size, primarily through boundary migration to reduce grain boundary energy per unit volume. During the plastic deformation of polycrystalline ice, the grains that are favorably oriented in the direction of the applied load deform by basal slip, that is, slip on the planes perpendicular to the c-axis. The load is then distributed to the grains with less favorable orientations, leading to the development of high stresses within those grains and causing a pronounced inhomogeneity in stress distribution (Duval et al., 1983; Humphreys & Hatherly, 2004). As a consequence of this stress inhomogeneity, the texture that is, size, shape, and arrangement of grains and fabric are altered during deformation, in a process known as dynamic recrystallization (DRX). DRX balances grain growth, maintaining a stable grain size in mid-depths, and occurs through different mechanisms. Bending stresses cause dislocation concentrations, resulting in polygonization or rotation recrystallization, which leads to negligible change in fabric (De La Chapelle et al., 1998; Duval & Castelnau, 1995). Migration recrystallization or strain-induced boundary migration (SIBM) occurs when low-dislocation-density grains bulge into neighboring high-dislocation-density grains, largely preserving the grain size and fabric (De La Chapelle et al., 1998; Duval et al., 1983). The bulging can lead to serrations in the grain boundaries that can serve as nucleation sites for new grains (Sakai et al., 2014). Nucleation and growth of new grains occurs when the dislocation density reaches a critical level, leading to oriented fabrics. The texture and fabric of ice evolve in response to the deformation rate, stress, and temperature, thereby preserving a history of the ice flow (Alley, 1988; Azuma & Higashi, 1985; Wilen et al., 2003). The constrained onset of DRX in firn may be of significance to adjusting model parameters for grain size evolution for the different stages of densification. Also, to our knowledge, no firn model has taken fabric that is, distribution of c-axis orientation of grains into consideration. Considering the effects of crystal orientation on firn may be crucial in improving the performance of firn models. An understanding of DRX processes in firn is critical to a comprehensive understanding of firn densification and the development of a widely acceptable, accurate firn densification law.

Understanding DRX in different materials is important for various reasons. In metals, it is essential in the automotive or aviation industries, where, for instance, it is used for grain refinement to make stronger and tougher metals and alloys (Wang et al., 2021; Zhang et al., 2022). In naturally deformed rocks, the relationship between the mean recrystallized grain size and flow stresses is used to constrain paleo-stresses (Stipp & Tullis, 2003; Twiss, 1977). In glaciers, DRX alters the microstructure of ice, which can strongly influence its mechanical properties such as strength, toughness, and ductility (Cole, 2001; Schulson, 1999). For instance, Ranganathan et al. (2021), via a model, demonstrated that large grain sizes in shear margins raise creep rate and ice fracture vulnerability.

Microstructural evolution of polar firn has previously been studied using microcomputed x-ray tomography (Burr et al., 2018; Freitag et al., 2004; Li & Baker, 2021; Lomonaco et al., 2011) and both optical microscopy and scanning electron microscopy (Kipfstuhl et al., 2009; Li & Baker, 2021). In previous studies, the role of DRX on densification and vice versa has been explored. Alley (1980), Alley et al. (1982), Gow (1969), Kipfstuhl et al., 2009, and Li and Baker (2021) observed DRX in polar firn, but none of the previous studies, to our knowledge, have been able to constrain its onset. In some recent studies, DRX in ice has been assumed to begin in the secondary creep regime (Chauve et al., 2015; Wilson et al., 2014). This is in contrast to some studies, where the onset of migration recrystallization has been observed to coincide with the onset of tertiary creep (De La Chapelle et al., 1998; Jacka, 1988) and a peak in the stress-strain curve (Duval et al., 1983), and other studies where DRX was observed to begin during primary creep, at 40%–95% of the strain required for strain rate minimum (Cross & Skemer, 2019). Montagnat et al. (2015) found that the activation of DRX mechanisms in ice results in the widely observed transition to tertiary creep at only 1% strain. However, firn has received comparatively less attention in this context.

This work presents a detailed analysis of the microstructural evolution and onset of recrystallization in samples of firn from 13 m depth at Summit, Greenland. We subjected the samples to a constant stress of 0.21 MPa and analyzed the microstructure and crystallographic orientations at different strains.

2. Materials and Methods

2.1. Firn Samples

The samples tested were extracted from an ~80 mm diameter, 80 m long firn core at Summit, Greenland (72°35′N, 38°25′W), with an average annual temperature of −31°C (Alley & Woods, 1996) and an average annual accumulation rate of 0.23 m.w.e a^{-1}. Drilled in June 2017, the core was cold shipped to the US Army Corps of Engineers Cold Region Research Engineering Laboratory (CRREL), Hanover, NH, where it was stored at −30°C. Four cylindrical samples, 22 ± 0.5 mm in diameter and 50 ± 0.5 mm in height, were cut from a section at a depth of 13 m, with their long axis cut parallel to the core axis using a hole saw and a band saw.

2.2. Creep Jigs

The samples were crept to strains of 7%, 12%, 18%, and 29% using custom-built creep jigs placed in a chest cooler (to avoid sublimation) in a cold room at −14 ± 0.5°C. The system, described by Li and Baker (2021), includes an aluminum base plate and three polished aluminum guard rails with linear bearings holding an upper loading plate (Figure S1 in Supporting Information S1). Displacement was measured using a calibrated Linear Voltage Displacement Transducer (LVDT) Omega LD-320 with 0.025% resolution and ±0.15% linearity error. The displacement was logged every 10 s with a Grant SQ2010 datalogger. Each sample was placed in the center of the plates, and a constant load corresponding to an engineering stress of 0.21 MPa—the same order of magnitude used by (Chauve, et al., 2015), was achieved by placing 8.16 kg of weights on the upper loading plate of the creep jig. After creep, all the samples remained cylindrical with no sign of localized deformation. Sample images are provided in Figure S2 in Supporting Information S1.

2.3. Thin Section Imaging

Two thin sections from the samples were imaged before and after creep. 2 mm thick sections were cut from the bulk specimens using a band saw and frozen to a glass plate. The thickness of the section was then reduced further to ~0.5 mm using a microtome. The thin section was then placed between a pair of cross-polarizing sheets on a light table, and optical micrographs were captured using a digital camera. All thin-section images can be viewed in Figures S3–S7 in Supporting Information S1.

2.4. Grain Area and Shape

Thin section images were analyzed using ImageJ (Schneider et al., 2012). The scale is set for each image, followed by drawing freeform lines around individual grains and measuring their area. The measured areas are then exported to a CSV file for further analysis. Visual depiction of the grain labeling and measurement process is provided in Figures S9 and S10 in Supporting Information S1. "Circularity" in ImageJ is used as a measure of grain sphericity for this work and is defined as follows:

$$C = \frac{4\pi \times A}{P^2}$$

Where A is the area and P is the perimeter of the grain. A value of 1 indicates a perfect circle. As the value approaches 0, it indicates an increasingly elongated grain. It is worth noting that circularity estimates may not be valid for very small grains, as it does not capture the full detail of their shapes.

To provide a quantitative analysis of the evolution of grain nucleation, a *recrystallized grain fraction* parameter has been defined as the ratio of the number of nucleated grains to the total number of grains:

$$\frac{\text{Number of nucleated grains}}{\text{Total number of grains}}$$

For simplicity, we have defined the number of nucleated grains as the number of grains with an area significantly smaller (<10%) than the average undeformed grain area.

2.5. Ice Fabrics

The fabrics (distribution of c-axis orientations) were obtained using a Rigsby (universal) stage, following the standard procedures described by Langway (1958). The stage is mounted between two cross-polaroids and has

four axes of rotation. Three of these axes are used to determine the orientation of the sample: the A1 axis for azimuth control and the other two axes (A2 and A4) for horizontal inclination. The fourth axis (A5) serves as a check and an axis of rotation for the whole stage.

These fabrics are subsequently plotted on a Schmidt plot, employing an equal area projection to map the c-axis orientation of each crystal onto the hemisphere of a circle.

2.6. X-Ray Microcomputed Tomography

2D and 3D reconstructions of the samples were obtained and characterized using a Bruker Skyscan 1172 housed in a −14°C cold room. The samples were scanned at an accelerating voltage of 40 KV and a current of 250 μA with an image pixel size of 17 μm. The samples were rotated 180° in the x-y plane between the X-ray source and a camera at 0.7° increments, producing 257 projection images.

The binary map images obtained from SkyScan software were then converted into grayscale images using the NRecon software. Next, using the CT-Analyzer (CTAn) software, the binary images were post-processed using techniques including filtering using anisotropic diffusion and despeckling. Quantitative 2D and 3D parameters were then measured.

Some microstructural parameters of interest include density, specific surface area (SSA), and the connectivity index (CI).

The specific surface area (SSA) is the surface-to-volume ratio of the firn sample, calculated using the hexahedral marching cubes method (Wang & Baker, 2013). For this study, we have defined SSA as the total surface area of the air-ice interface per kg of ice.

The connectivity index is the ratio of the volume of the largest pore ($V_{\text{largest\_pore}}$) to the total volume of pores:

$$\text{CI} = \frac{V_{\text{largest\_pore}}}{V_{\text{pores}}}$$

This metric has previously been used by Martin et al. (2000) in characterizing cavity coalescence during the superplastic deformation of an aluminum alloy, Babin et al. (2006) in depicting void coalescence in bread, and Burr et al. (2018) in quantifying pore morphology in polar firn.

The connectivity index is close to 1 when the pore network is almost fully interconnected and close to 0 when all pores are closed. A notable advantage of using the connectivity index to quantify pore morphology over other methods is its robustness to the volume of the sample and image resolution.

The density of the samples was calculated as described by Wang and Baker (2013), using the percent object volume, which is the ratio of volume occupied by ice (Obj. V), to the total volume of firn including voids (TV). The density is calculated as follows:

$$\rho_{\{\text{firn}\}} = \frac{\text{Obj.}V}{\text{TV}}\rho_{\{\text{ice}\}}$$

Where $\rho_{\{\text{ice}\}}$ is the theoretical density of pure ice (917 kgm^{-3}).

3. Results and Observations

Four compression tests were conducted under a constant stress of 0.21 MPa at −14°C. The tests were terminated at strains of 7%, 12%, 18%, and 29% respectively. To analyze the microstructural evolution of the firn over time, we used four separate samples with similar initial characteristics. Figure 1a shows the strain-versus-time curve, and Figure 1b shows the strain rate-versus-strain curve for the samples at their respective strains. Figure 1b shows a clear transition from decelerating (transient) creep to secondary creep at strains ranging from 7% to 14%.

Figure 1b shows the strain rate-versus-strain plot for all specimens. An average minimum strain rate of 10^{-7} s^{-1} is reached at strains ranging from 7% to 14% across all the samples. The slight differences in strain rates and points of minimum strain rate observed in Figure 1b are thought to be a result of slight differences in initial microstructures and sample dimensions, as well as variations in the equalization of the load train.

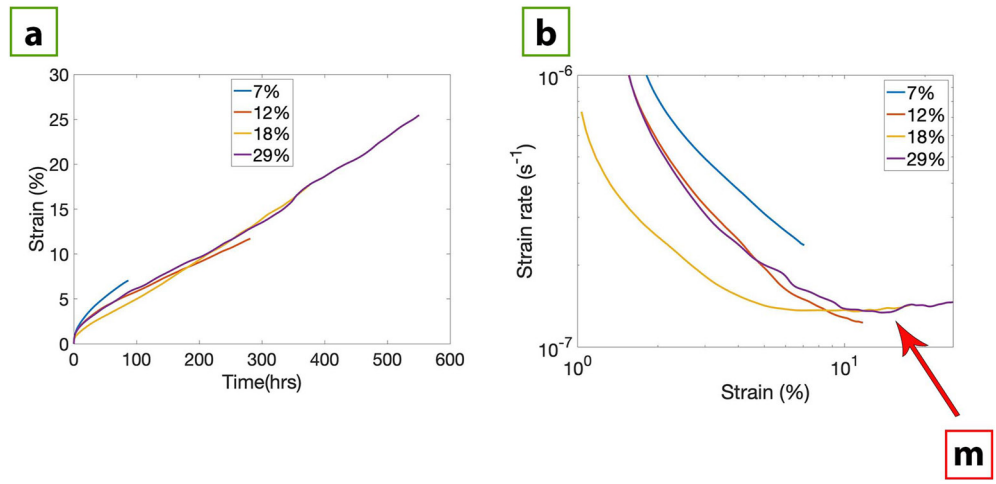

Figure 1. Curves of (a) strain versus time, (b) strain rate versus strain of the 13 m firn sample crept to 29% under an applied engineering stress of 0.21 MPa. "m" indicates the point of minimum strain rate, beyond which the strain rate slightly increases, indicating the onset of secondary creep.

3.1. Grain Shape and Size

Polarized light images of thin sections of all specimens are shown in Figure 2a. All test samples initially had equiaxed grains with an average grain size of ~1 mm^2. A transition from equiaxed to elongated grains, visually observed in Figure 2a as well as in the sharp decrease in sphericity (Figure 3f), is observed at 7%, followed by grain shape stabilization which is related to the nucleation of finer grains at about 12%.

The median grain area decreases significantly at 7% strain, and stabilizes after 12% strain, as shown in Figure 3e. The evolution of grain area distribution as a function of strain is presented in Figure 2c. The distribution trends from normal in the undeformed sample to bimodal in the strained samples. Figure 3d illustrates the trend in the *recrystallized grain fraction* parameter The data demonstrates a rising rate of recrystallization with increasing strain.

3.2. Crystal Orientation

C-axis orientations were obtained at strains of 0%, 7%, 12%, 18%, and 29% using the Universal stage. Figure 2b shows stereographic projections for the c-axis orientations of grains in each specimen.

In Figure 2b, the Schmidt nets indicate an initial random distribution of c-axis orientations at low strains, with a few grains indicating horizontal c-axes at 0%. Around 7% strain, just before reaching the minimum strain rate, while the fabric remains random, a slow clustering process begins with the disappearance of horizontally oriented grains.

At 12% strain, the clustering process continues as more c-axis orientations converge toward the center of the Schmidt net, indicating a developing fabric. This trend strengthens at 18% strain. Finally, at 29% strain, a cluster of vertical c-axis orientations appears, centered around the plot's origin, corresponding to the compression direction.

3.3. Micro-CT Reconstructions

Figure 2d presents 2D cross-sections of all samples, where the ice appears white and the pores are black. This 2D reconstruction visually captures the coarsening of the firn samples as is evident in the rounding of pores and the reduction in porosity as the strain increases.

In Figures 3a and 3b, the trends in density and SSA are depicted as strain increases. The density increases by 30% between the undeformed sample and the sample deformed to 29% strain. The SSA decreases as the density increases, consistent with the densification of polar firn.

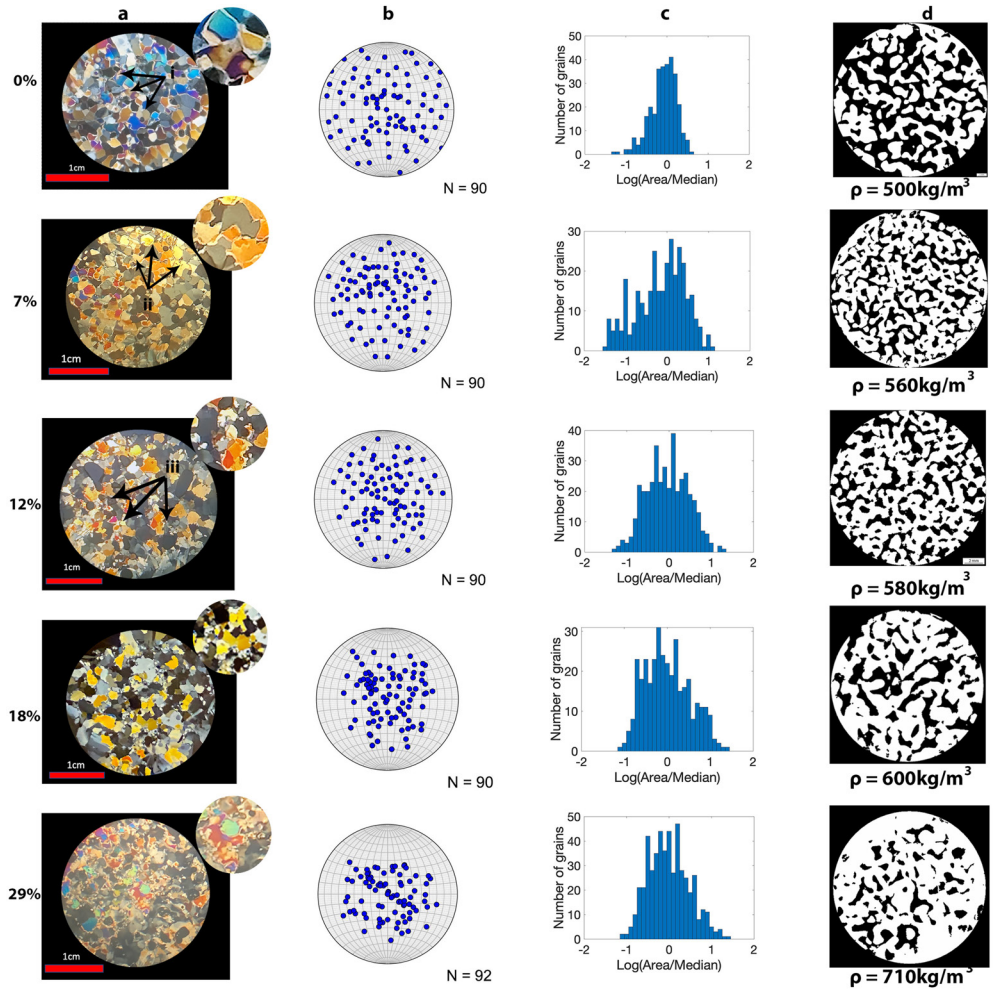

Figure 2. (a) Polarized light images (i) indicates the equiaxed grains, (ii) indicates the elongated grains, and (iii) indicates the nuclei of recrystallized grains(b) C-axis pole figures from individual grains represented on a Schmidt net. Each point on the Schmidt net corresponds to the orientation of one individual crystal. A crystal with a vertical c-axis has a point at the center of the plot, while a crystal with a horizontal c-axis has a point at the edge of the plot. (c) Logarithmic distributions of grain area (mm^2) (d) Micro-CT 2D reconstructions of horizontal thin sections (white indicates ice, black indicates air) of 13 m firn samples as compression strain increases from 0% at the top to 29% at the bottom.

In Figure 3c, the change in CI is depicted as strain increases. CI decreases by ∼8% from the undeformed sample to the sample deformed to 29% strain, with the most significant decrease occurring between 18% strain (600 Kgm^{-3}) and 29% strain (710 Kgm^{-3}).

4. Discussion

The second stage of densification, occurring at densities between 550 Kgm^{-3} and 830 Kgm^{-3}, is controlled by deformation and recrystallization. SIBM can occur when the strain energy difference between adjacent grains is enough to nucleate a bulge in the grain boundary (Duval et al., 1983). Unlike rotation recrystallization and nucleation and growth, SIBM does not involve the formation of new crystals, instead, it leads to the migration of grain boundaries (Reed-Hill & Abbaschian, 2008). In our tested samples, DRX is observed during the transition from primary creep to secondary creep with SIBM starting at 7% strain, and nucleation of a few new grains commencing before 12% strain. This process continues up to ∼29% strain, resulting in substantial recrystallization and an 85% reduction in median grain area.

As the sample is deformed to 29% strain, the median grain area exhibits a decreasing rate of reduction, indicating substantial recrystallization. Part of the annealing process in ice involves normal grain growth. Carpenter and

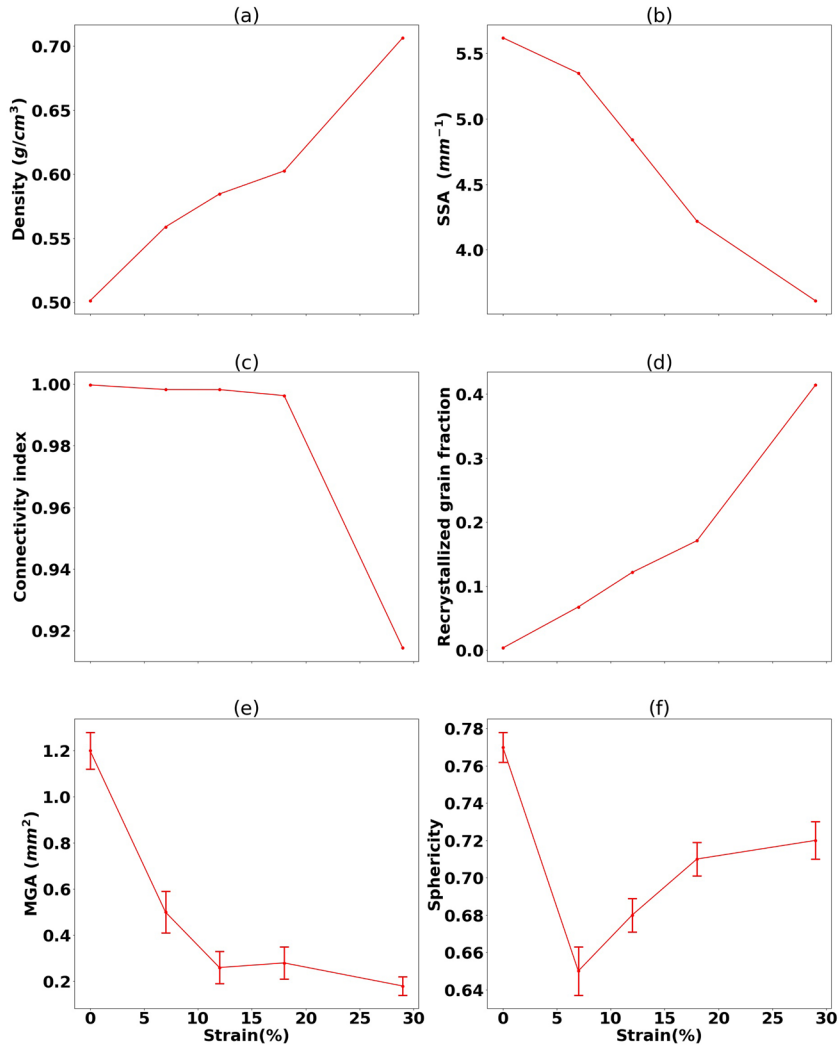

Figure 3. Trends in microstructural parameters: (a) density, (b) specific surface area (SSA), (c) Connectivity index (d) Recrystallized grain fraction (e) Median grain area (MGA), and (f) sphericity for samples strained to 0%, 7%, 12%, 18%, and 29%.

Elam (1920) and Altherthum (1922) established the distinguishing factor between recrystallization and grain growth, stating that the driving force for recrystallization is provided by stored energy and that for grain growth is provided by grain boundary energy (Humphreys & Hatherly, 2004). If deformation is continued to larger strains, it is still unclear whether there is a transition or a balance between recrystallization and normal grain growth. This phenomenon is worthy of further study.

The evolution of grain size distribution with strain (Figure 2c) shows a transition from a normal distribution in the unstrained sample to a bimodal distribution in the rest of the samples. The grain area evolution is also described by the recrystallized grain fraction which increases from ~6% to ~40% as the strain increases from 7% to 29%. These observations indicate an increase in the volume fraction of recrystallized material as the strain increases.

The grains start becoming elongated with serrated boundaries at ~7% (Figure 2a). This change in grain shape is associated with a decrease in sphericity which has been linked to reduced porosity and permeability in rocks (Payton et al., 2022; Safari et al., 2021). Also, Figure 3 shows that as the grain size decreases, the density increases. Smaller grains have a larger surface area per unit volume than larger grains, resulting in greater interactions between grains.

In addition to density and grain size evolution, other structural parameters such as SSA and CI contribute further to understanding the microstructural evolution (Figure 3). Consistent with the densification of polar firn, SSA

and CI decrease with increasing density. While CI remains close to 1, it notably declines between 18% and 29% strain (between 600 Kgm^{-3} and 710 Kgm^{-3}). This is consistent with the findings of Burr et al. (2018) who found that pores in polar firn remain well interconnected with a CI value close to 1, up to the pore close-off density of ~830 Kgm^{-3} beyond which CI significantly drops to ~0. While these parameters are evidence of microstructural evolution, no significant change in their values points to the onset of recrystallization.

In Figure 2b, the fabrics of the grains indicate random orientations up to around ~7% strain, when a slow clustering process is observed. At this point, no horizontal grain orientations are observed, and there is a slight convergence toward the compression axis, which becomes more pronounced with increasing strain. This fabric development aligns with the findings of Azuma and Higashi (1985), who determined that the compression of a sample with a random fabric results in clustering around the compression axis. Preferred crystal orientation records deformational history (Alley, 1988), and results in increased plastic anisotropy in glacier ice, affecting its flow in glaciers and ice sheets. Furthermore, fabric and texture contrasts across different climate change events are believed to cause significant variations in the rheology of ice in different ice cores (Azuma et al., 2000; Durand et al., 2007; Paterson, 1991; Saruya et al., 2022; Thorsteinnson et al., 1997). For instance, Paterson (1991) found that the strong, near-vertical single maximum fabric in ice-age ice, keeps the grain size small and leads to a strain rate 2.5 times faster than that in Holocene ice under the same stress and temperature. Therefore, the fabric development observed in this study may impact subsequent grain size evolution and, consequently, the flow rate of firn.

Many firn models either neglect grain size evolution or focus on grain growth mechanisms (Arthern et al., 2010; Kingslake et al., 2022). However, these models that consider grain growth have failed to demonstrate significant improvement in their performance (Stevens et al., 2020). Our findings, supported by other studies (Durand et al., 2008; Kipfstuhl et al., 2009) indicate that while some grains grow, SIBM and the nucleation of finer grains also occur in firn. This highlights the need for incorporating additional grain size evolution theories, such as DRX in addition to normal grain growth (NGG) during firn densification, underscoring the important role DRX mechanisms will play in the development of a physics-based firn model.

5. Conclusion

We have subjected firn from a depth of 13 m to deformation by compressive creep to various strains, ranging from 7% to 29%. We examined the resulting microstructures using a combination of micro-CT and optical microscopy techniques. We have demonstrated that DRX occurs in low-density firn, with the onset in the present case occurring around 7% strain, coinciding with the onset of secondary creep. The recrystallization leads to elongated grains with serrated boundaries, a reduction in median grain size, and a change in the fabric, indicating that recrystallization occurs by SIBM, and nucleation and growth. These findings underscore the importance of considering DRX mechanisms (SIBM, nucleation, and growth) to comprehensively understand and model firn densification.

Of further interest is the effect of temperature on the recrystallization mechanisms present during firn densification. Higher temperatures at high strain can lead to faster grain boundary migration rates, which may result in the domination of SIBM during DRX (De La Chapelle et al., 1998; Thorsteinnson et al., 1997). At relatively lower strains, higher temperatures provide more thermal energy, facilitating nucleation and subsequent growth (Humphreys & Hatherly, 2004). Consequently, higher temperatures might trigger an earlier onset of DRX. Therefore, the effects of temperature on DRX mechanisms in firn are worthy of further study.

Acknowledgments
This work was sponsored by the National Science Foundation Office of Polar Programs (Antarctic Glaciology) Grant 1851094. We thank Chris Polashenski, Zoe Courville, and Lauren B. Farnsworth at CRREL for help with the firn core storage. We appreciate all the valuable discussions, comments, and suggestions provided by TJ Fudge, Colin Meyer, and Jacob Buffo to help us improve the quality of this manuscript. We also acknowledge the use of the Ice Research Laboratory (Director-E.M. Schulson) at Dartmouth College.

Data Availability Statement

The mechanical and microstructural data supporting the conclusions in this study are available at Ogunmolasuyi et al. (2023).

References

Alley, R. B. (1980). *Densification and recrystallization of firn at Dome C, East Antarctica* (p. 77). Institute of Polar Studies, Ohio State University, Report.

Alley, R. B. (1987). Firn densification by grain-boundary sliding: A first model. *Journal de Physique Colloques*, *48*(C1), C1-249–C1-256. https://doi.org/10.1051/jphyscol:1987135

Alley, R. B. (1988). Fabrics in polar ice sheets: Development and prediction. *Science*, *240*(4851), 493–495. https://doi.org/10.1126/science.240.4851.493
Alley, R. B. (2000). *The two-mile time machine: Ice cores, abrupt climate change, and our future*. Princeton University Press.
Alley, R. B., Bolzan, J. F., & Whillans, I. M. (1982). Polar firn densification and grain growth. *Annals of Glaciology*, *3*, 7–11. https://doi.org/10.3189/s0260305500002433
Alley, R. B., & Woods, G. A. (1996). Impurity influence on normal grain growth in the GISP2 ice core, Greenland. *Journal of Glaciology*, *42*(141), 255–260. https://doi.org/10.3189/s0022143000004111
Alterthum, H. (1922). Zur Theorie der Rekristallisation. *Zeitschrift Für Elektrochemie Und Angewandte Physikalische Chemie*, *28*(15–16), 347–356. https://doi.org/10.1002/bbpc.19220281504
Arnaud, L., Barnola, J., & Duval, P. (2000). Physical modeling of the densification of snow/firn and ice in the upper part of polar ice sheets. *Physics of Ice Core Records*. http://hdl.handle.net/2115/32472
Arthern, R. J., Vaughan, D. G., Rankin, A. M., Mulvaney, R., & Thomas, E. R. (2010). In situ measurements of Antarctic snow compaction compared with predictions of Models. *Journal of Geophysical Research*, *115*(F3), F03011. https://doi.org/10.1029/2009jf001306
Azuma, N., & Higashi, A. (1985). Formation processes of ice fabric pattern in ice sheets. *Annals of Glaciology*, *6*, 130–134. https://doi.org/10.3189/1985aog6-1-130-134
Azuma, N., Wang, Y., Yoshida, Y., Narita, H., Hondoh, T., Shoji, H., & Watanabe, O. (2000). Crystallographic analysis of the Dome Fuji ice core.
Babin, P., Della Valle, G., Chiron, H., Cloetens, P., Hoszowska, J., Pernot, P., et al. (2006). Fast X-ray tomography analysis of bubble growth and foam setting during breadmaking. *Journal of Cereal Science*, *43*(3), 393–397. https://doi.org/10.1016/j.jcs.2005.12.002
Barnola, J. M., Pimienta, P., Raynaud, D., & Korotkevich, Y. S. (1991). CO_2-climate relationship as deduced from the Vostok ice core: A re-examination based on new measurements and on a re-evaluation of the air dating. *Tellus B: Chemical and Physical Meteorology*, *43*(2), 83–90. https://doi.org/10.1034/j.1600-0889.1991.t01-1-00002.x
Burr, A., Ballot, C., Lhuissier, P., Martinerie, P., Martín, C., & Philip, A. (2018). Pore morphology of polar firn around closure revealed by X-ray tomography. *The Cryosphere*, *12*(7), 2481–2500. https://doi.org/10.5194/tc-12-2481-2018
Carpenter, H. C. H., & Elam, C. F. (1920). Crystal growth and recrystallization in metals. *Journal of the Institute of Metals*, *24*.
Chauve, T., Montagnat, M., & Vacher, P. (2015). Strain field evolution during dynamic recrystallization nucleation; a case study on Ice. *Acta Materialia*, *101*, 116–124. https://doi.org/10.1016/j.actamat.2015.08.033
Cole, D. M. (2001). The microstructure of ice and its influence on mechanical properties. *Engineering Fracture Mechanics*, *68*(17–18), 1797–1822. https://doi.org/10.1016/s0013-7944(01)00031-5
Cross, A. J., & Skemer, P. (2019). Rates of dynamic recrystallization in geologic materials. *Journal of Geophysical Research: Solid Earth*, *124*(2), 1324–1342. https://doi.org/10.1029/2018jb016201
De La Chapelle, S., Castelnau, O., Lipenkov, V., & Duval, P. (1998). Dynamic recrystallization and texture development in ice as revealed by the study of deep ice cores in Antarctica and Greenland. *Journal of Geophysical Research*, *103*(B3), 5091–5105. https://doi.org/10.1029/97jb02621
Durand, G., Gillet-Chaulet, F., Svensson, A., Gagliardini, O., Kipfstuhl, S., Meyssonnier, J., et al. (2007). Change in ice rheology during climate variations—Implications for ice flow modelling and dating of the Epica Dome C Core. *Climate of the Past*, *3*(1), 155–167. https://doi.org/10.5194/cp-3-155-2007
Durand, G., Persson, A., Samyn, D., & Svensson, A. (2008). Relation between neighbouring grains in the upper part of the Northgrip ice core—Implications for rotation recrystallization. *Earth and Planetary Science Letters*, *265*(3–4), 666–671. https://doi.org/10.1016/j.epsl.2007.11.002
Duval, P., Ashby, M. F., & Anderman, I. (1983). Rate-controlling processes in the creep of polycrystalline ice. *Journal of Physical Chemistry*, *87*(21), 4066–4074. https://doi.org/10.1021/j100244a014
Duval, P., & Castelnau, O. (1995). Dynamic recrystallization of ice in polar ice sheets. *Journal de Physique*, *IV*(C3), 05–C3-205. https://doi.org/10.1051/jp4:1995317
Forster, R. R., Box, J. E., van den Broeke, M. R., Miège, C., Burgess, E. W., van Angelen, J. H., et al. (2013). Extensive liquid meltwater storage in firn within the Greenland Ice Sheet. *Nature Geoscience*, *7*(2), 95–98. https://doi.org/10.1038/ngeo2043
Freitag, J., Wilhelms, F., & Kipfstuhl, S. (2004). Microstructure-dependent densification of polar firn derived from X-ray microtomography. *Journal of Glaciology*, *50*(169), 243–250. https://doi.org/10.3189/172756504781830123
Gow, A. J. (1969). On the rates of growth of grains and crystals in South Polar Firn. *Journal of Glaciology*, *8*(53), 241–252. https://doi.org/10.3189/s0022143000031233
Gow, A. J. (1975). Time dependent sintering of perennial isothermal snowpacks. *International Association of Hydrological Sciences*, *114*.
Harper, J., Humphrey, N., Pfeffer, W. T., Brown, J., & Fettweis, X. (2012). Greenland ice-sheet contribution to sea-level rise buffered by meltwater storage in firn. *Nature*, *491*(7423), 240–243. https://doi.org/10.1038/nature11566
Helsen, M. M., van den Broeke, M. R., van de Wal, R. S., van de Berg, W. J., van Meijgaard, E., Davis, C. H., et al. (2008). Elevation changes in Antarctica mainly determined by accumulation variability. *Science*, *320*(5883), 1626–1629. https://doi.org/10.1126/science.1153894
Herron, M. M., & Langway, C. C. (1980). FIRN densification: An empirical model. *Journal of Glaciology*, *25*(93), 373–385. https://doi.org/10.1017/s0022143000015239
Horlings, A. N., Christianson, K., Holschuh, N., Stevens, C. M., & Waddington, E. D. (2021). Effect of horizontal divergence on estimates of firn-air content. *Journal of Glaciology*, *67*(262), 287–296. https://doi.org/10.1017/jog.2020.105
Humphreys, F. J., & Hatherly, M. (2004). *Recrystallization and related annealing phenomena*. Elsevier.
Jacka, T. H. (1988). *Experimental investigations of the flow of ice*. Ph.D. thesis, University of Melbourne.
Kingslake, J., Skarbek, R., Case, E., & McCarthy, C. (2022). Grain-size evolution controls the accumulation dependence of modelled firn thickness. *The Cryosphere*, *16*(9), 3413–3430. https://doi.org/10.5194/tc-16-3413-2022
Kipfstuhl, S., Faria, S. H., Azuma, N., Freitag, J., Hamann, I., Kaufmann, P., et al. (2009). Evidence of dynamic recrystallization in polar firn. *Journal of Geophysical Research*, *114*(B5), B05204. https://doi.org/10.1029/2008jb005583
Langway, C. C. (1958). Ice fabrics and the universal stage. In *U.S. Army snow, ice and permafrost research establishment*. Technical Report 62.
Li, Y., & Baker, I. (2021). Observations of the creep of polar firn. *Journal of Glaciology*, *68*(268), 1–19. https://doi.org/10.1017/jog.2021.91
Lomonaco, R., Albert, M., & Baker, I. (2011). Microstructural evolution of fine-grained layers through the firn column at Summit, Greenland. *Journal of Glaciology*, *57*(204), 755–762. https://doi.org/10.3189/002214311797409730
Maeno, N., & Ebinuma, T. (1983). Pressure sintering of ice and its implication to the densification of snow at Polar Glaciers and ice sheets. *Journal of Physical Chemistry*, *87*(21), 4103–4110. https://doi.org/10.1021/j100244a023
Martin, C. F., Josserond, C., Salvo, L., Blandin, J. J., Cloetens, P., & Boller, E. (2000). Characterisation by X-ray micro-tomography of cavity coalescence during superplastic deformation. *Scripta Materialia*, *42*(4), 375–381. https://doi.org/10.1016/s1359-6462(99)00355-3
Meyer, C. R., Keegan, K. M., Baker, I., & Hawley, R. L. (2020). A model for French-press experiments of dry snow compaction. *The Cryosphere*, *14*(5), 1449–1458. https://doi.org/10.5194/tc-14-1449-2020

Montagnat, M., Chauve, T., Barou, F., Tommasi, A., Beausir, B., & Fressengeas, C. (2015). Analysis of dynamic recrystallization of ice from EBSD orientation mapping. *Frontiers in Earth Science*, *3*. https://doi.org/10.3389/feart.2015.00081

Ogunmolasuyi, A., Murdza, A., & Baker, I. (2023). The onset of recrystallization in polar firn, summit, Greenland, June 2017 [Dataset]. Arctic Data Center. https://doi.org/10.18739/A21R6N25H

Oraschewski, F. M., & Grinsted, A. (2022). Modeling enhanced firn densification due to strain softening. *The Cryosphere*, *16*(7), 2683–2700. https://doi.org/10.5194/tc-16-2683-2022

Paterson, W. S. B. (1991). Why ice-age ice is sometimes "soft.". *Cold Regions Science and Technology*, *20*(1), 75–98. https://doi.org/10.1016/0165-232x(91)90058-o

Payton, R. L., Chiarella, D., & Kingdon, A. (2022). The influence of grain shape and size on the relationship between porosity and permeability in sandstone: A digital approach. *Scientific Reports*, *12*(1), 7531. https://doi.org/10.1038/s41598-022-11365-8

Ranganathan, M., Minchew, B., Meyer, C. R., & Peč, M. (2021). Recrystallization of ice enhances the creep and vulnerability to fracture of ice shelves. *Earth and Planetary Science Letters*, *576*, 117219. https://doi.org/10.1016/j.epsl.2021.117219

Raynaud, D., Jouzel, J., Barnola, J. M., Chappellaz, J., Delmas, R. J., & Lorius, C. (1993). The ice record of Greenhouse gases. *Science*, *259*(5097), 926–934. https://doi.org/10.1126/science.259.5097.926

Reed-Hill, R. E., & Abbaschian, R. (2008). *Physical metallurgy principles*. Thomson.

Safari, M., Gholami, R., Jami, M., Ananthan, M. A., Rahimi, A., & Khur, W. S. (2021). Developing a porosity-permeability relationship for ellipsoidal grains: A correction shape factor for Kozeny-Carman's equation. *Journal of Petroleum Science and Engineering*, *205*, 108896. https://doi.org/10.1016/j.petrol.2021.108896

Sakai, T., Belyakov, A., Kaibyshev, R., Miura, H., & Jonas, J. J. (2014). Dynamic and post-dynamic recrystallization under hot, cold and severe plastic deformation conditions. *Progress in Materials Science*, *60*, 130–207. https://doi.org/10.1016/j.pmatsci.2013.09.002

Saruya, T., Fujita, S., Iizuka, Y., Miyamoto, A., Ohno, H., Hori, A., et al. (2022). Development of crystal orientation fabric in the Dome Fuji ice core in East Antarctica: Implications for the deformation regime in ice sheets. *The Cryosphere*, *16*(7), 2985–3003. https://doi.org/10.5194/tc-16-2985-2022

Schneider, C. A., Rasband, W. S., & Eliceiri, K. W. (2012). NIH image to ImageJ: 25 years of image analysis. *Nature Methods*, *9*(7), 671–675. https://doi.org/10.1038/nmeth.2089

Schulson, E. M. (1999). The structure and mechanical behavior of Ice. *JOM*, *51*(2), 21–27. https://doi.org/10.1007/s11837-999-0206-4

Sowers, T., & Bender, M. (1995). Climate records covering the last deglaciation. *Science*, *269*(5221), 210–214. https://doi.org/10.1126/science.269.5221.210

Stevens, C. M., Verjans, V., Lundin, J. M., Kahle, E. C., Horlings, A. N., Horlings, B. I., & Waddington, E. D. (2020). The community firn model (CFM) v1.0. *Geoscientific Model Development*, *13*(9), 4355–4377. https://doi.org/10.5194/gmd-13-4355-2020

Stipp, M., & Tullis, J. (2003). The recrystallized grain size piezometer for Quartz. *Geophysical Research Letters*, *30*(21), 6667–6674. https://doi.org/10.1029/2003gl018444

Thorsteinsson, T., Kipfstuhl, J., & Miller, H. (1997). Textures and fabrics in the grip ice core. *Journal of Geophysical Research*, *102*(C12), 26583–26599. https://doi.org/10.1029/97jc00161

Twiss, R. J. (1977). Theory and applicability of a recrystallized grain size paleopiezometer. *Stress in the Earth*, 227–244. https://doi.org/10.1007/978-3-0348-5745-1_13

Wang, S., Xu, W., Wu, H., Yuan, R., Jin, X., & Shan, D. (2021). Simulation of dynamic recrystallization of a magnesium alloy with a cellular automaton method coupled with adaptive activation energy and matrix deformation topology. *Manufacturing Review*, *8*, 11. https://doi.org/10.1051/mfreview/2021009

Wang, X., & Baker, I. (2013). Observation of the microstructural evolution of snow under uniaxial compression using X-ray computed microtomography. *Journal of Geophysical Research: Atmospheres*, *118*(22), 12371–12382. https://doi.org/10.1002/2013jd020352

Wilen, L. A., Diprinzio, C. L., Alley, R. B., & Azuma, N. (2003). Development, principles, and applications of automated ice fabric analyzers. *Microscopy Research and Technique*, *62*(1), 2–18. https://doi.org/10.1002/jemt.10380

Wilson, C. J. L., Peternell, M., Piazolo, S., & Luzin, V. (2014). Microstructure and fabric development in ice: Lessons learned from in situ experiments and implications for understanding rock evolution. *Journal of Structural Geology*, *61*, 50–77. https://doi.org/10.1016/j.jsg.2013.05.006

Zhang, D., Dong, X. J., Xu, Y., Tu, Z. L., Lu, S. Q., & Gong, S. H. (2022). Study on dynamic recrystallization mechanism and model of tb15 titanium alloy. *IOP Conference Series: Materials Science and Engineering*, *1270*(1), 012072. https://doi.org/10.1088/1757-899x/1270/1/012072